Supporting Information

Aruda et al. 10.1073/pnas.1222327110

SI Text

Synthesis of Hexadecylamine-Coated Gold Nanoparticles. We used an adapted procedure to synthesize hexadecylamine-coated gold nanoparticles (HDA-AuNPs) (1). Before use, we cleaned all glassware and stir bars with aqua regia [75% (vol/vol) hydrochloric acid and 25% (vol/vol) nitric acid], rinsed each piece thoroughly with 18 MΩ Millipore water, and then dried each piece in a 125 °C drying oven. In brief, we stirred a mixture of 8 g (34 mmol) of hexadecylamine (≈90%; Aldrich) and 15 mL of toluene (Aldrich) vigorously in a 100-mL round-bottom flask for 15 min. To this mixture, we added a solution of 0.66 g (1.7 mmol) of hydrogen tetrachloroaurate (III) trihydrate (≥99.9%; Aldrich) and 5 g (21 mmol) of hexadecylamine in 45 mL of toluene and stirred for an additional 10 min. Under continued stirring, we added 6 mL of methanol, followed by 0.12 g (3.2 mmol) of sodium borohydride (Aldrich).

Immediately after the addition of sodium borohydride, the solution turned a deep purple color, which is an indication of HDA-AuNPs formation. We stirred the solution for an additional 2 h. The particles were purified from the solvents and excess reagents by two cycles of methanol-induced precipitation, centrifugation (spun at 3,200 rpm with a Heraeus Instruments rotor #8179 for 3 min), and resolubilization in clean toluene. To prepare the particles for further characterization, we filtered the solution with a 250-nm Whatman syringe filter, precipitated the nanoparticles once more in methanol, and then resolubilized the dried nanoparticles in an oxygen-free (freeze-pump-thawed) 10 mM hexadecylamine solution in toluene (50 mL) in a sealed nitrogen glove box.

Generation of Hexadecanethiol-Coated AuNPs and Sample Preparation. To generate samples of aminated (HDA-AuNPs) and thiolated hexadecanethiol-coated AuNPs (HDT-AuNPs) nanoparticles of similar optical density and hexadecylamine ligand concentration, we (*i*) dispensed 1,000 μL of the aminated AuNPs into eight separate silanized (Rain-X) glass vials, (*ii*) added 3,000 μL of oxygen-free 10 mM hexadecylamine in toluene to the first four vials (A1–A4) to generate HDA-AuNPs, and (*iii*) added 3,000 μL of oxygen-free 10 mM hexadecylamine/1 mM hexadecanethiol in toluene (~150% of the amount needed to achieve full surface coverage of hexadecanethiol onto all AuNPs) to the last four vials (T1–T4) to generate HDT-AuNPs. We allowed the particles to equilibrate/ligand exchange with the additional ligands for 4 d in the nitrogen box and then filtered the solutions with a 250-nm Whatman syringe filter to remove agglomerates. We obtained the average diameter of the nanoparticles by transmission electron microscopy (TEM) analysis (JOEL JEM-2100F FAST TEM) of n = 2,689 NPs for the aminated Au NPs and n = 2,026 NPs for thethiolated Au NPs using ImageJ analysis software (Fig. S1). The average diameter of the aminated Au NPs was 3.6 ± 0.7 nm, and the average diameter of the thiolated Au NPs was 3.2 ± 0.6 nm.

To prepare transient absorption (TA) samples, we diluted each solution with additional 10 mM HDA in toluene in a 0.2-mm TA cuvette to an OD of ~0.5 at the peak plasmon resonance wavelength (Fig. S2). We then determined the extinction coefficient for each solution by Beer's law analysis of the spectrum at 520 nm (Eq. **S1**) as follows:

$$\varepsilon = \frac{A}{bC}, \qquad \textbf{[S1]}$$

where A is the absorbance, ε is the extinction coefficient (in molar^{-1}·centimeter^{-1}), b is the path length of the cuvette (in centimeters), and C is the concentration of the nanoparticles (in moles of Au NPs per liter), as determined by inductively coupled plasma atomic emission spectroscopy (ICP-AES) (Varian VISTA ICP OES) and the average size (from TEM analysis).

Samples for ICP-AES were prepared by (*i*) precipitating nanoparticles (A1–A4, T1–T4) of known volume and absorbance spectrum with a 5-mL portion of methanol or acetone, (*ii*) centrifuging them at 11,000 rpm with a Heraeus Instruments rotor #8179 for 20 min (*iii*) decanting the solvents, (*iv*) dissolving the particles in a 1,000-μL portion of aqua regia, and (*v*) diluting the solution to a final volume of 10.00 mL with 18 MΩ Millipore water. We then compared the samples to commercially available gold standards (TraceCERT; 1,000 mg/L Au in hydrochloric acid; Fluka). The average extinction coefficient obtained for aminated Au NPs (A1–A4) was $4.71 \times 10^6 \pm 0.04 \times 10^6$ M^{-1}·cm^{-1} and for the thiolated Au NPs (T1–T4) was $3.07 \times 10^6 \pm 0.07 \times 10^6$ M^{-1}·cm^{-1}.

Table S1 summarizes the wavelengths of the localized surface plasmon resonance (LSPR) peak and extinction coefficient at this wavelength for each sample.

In the TA experiments, the laser power is tuned to achieve the absorption of a specific number of photons at the excitation wavelength of the pump laser (520 nm) per particle, where the number of photons absorbed per nanoparticle is Poisson-distributed with mean $\langle N \rangle$. In determining $\langle N \rangle$, we account for the relative absorption coefficients of the two types of samples at 520 nm, and we include the contribution of the d-sp interband transition to the total absorption.

Effect of Etching of the Particles on Integrated Absorption Coefficient. The localized surface plasmon (LSP) absorption of Au NPs, unlike Ag NPs, overlaps with the d-sp interband transition, so we determined the integrated absorption coefficient for the plasmon peak by first subtracting a spline background from the spectrum (Fig. S3). We integrated over the energy of the absorption feature (in units of electron volts) to determine an integrated absorption coefficient of 2.2×10^5 (M^{-1}·cm^{-1}·eV) for the aminated particles and 1.9×10^5 (M^{-1}·cm^{-1}·eV) for the thiolated particles. Note that the decrease in oscillator strength from aminated to thiolated particles is consistent with the slight etching of the particles observed in the TEM—that is, the reduction in volume from aminated to thiolated Au NPs is consistent with the observed reduction in oscillator strength.

Transient Absorption Measurements. We split the 2.5-mJ output of a commercial amplified Ti-sapphire laser (Solstice; 1 kHz, 100 fs; Spectra Physics), and guided 95% to an optical parametric amplifier (TOPAS-C; Light Conversion) used to produce the pump wavelength for sample excitation, and 5% to a commercial TA spectrometer (Helios; Ultrafast Systems) for use as the probe. Within the spectrometer, a single-filament broadband continuum of wavelengths from 420 to 720 nm was generated in a sapphire plate. The pump and probe were recombined at the sample in a 2-mm quartz cuvette. The pump spot size was expanded to greater than twice the size of the probe spot to compensate for any imperfections in translation stage alignment. All samples were prepared with an absorbance of 0.5 ± 0.03 OD at the maximum of the LSP absorption feature. The transmitted probe signal was passed through a 750-nm short-wave pass filter and collected in optical fiber. The output of the fiber was dispersed onto an array detector. The output differential absorption spectrum (ΔA) was

obtained through active background subtraction of the ground-state (GS) spectrum by chopping the pump at 500 Hz. The instrument response, given by the cross-correlation of the pump and probe, was measured by inducing the optical Kerr effect in a quartz microscope coverslip at the position of the sample, and it was found that the instrument response function of the system is 200 fs.

Fitting of the GS and TA Spectra. To fit the GS and TA spectra, we need to simulate the spectrum of the gold nanoparticle solution for different electronic temperatures (T_e). This simulation was performed using the quasistatic approximation for the absorption coefficient (Q_{abs}) of a spherical particle of complex dielectric function $\varepsilon(T_e)$ in an infinite medium of dielectric function ε_m (2, 3). The absorption coefficient is given by Eq. **S2**:

$$Q_{abs} = C\frac{a}{\lambda}\frac{\varepsilon''(T_e)}{\varepsilon''(T_e)^2 + \left(\varepsilon'(T_e) + 2\varepsilon_m\right)^2}, \qquad \textbf{[S2]}$$

where C is a constant, a is the radius of the NP, and $\varepsilon'(T_e)$ and $\varepsilon''(T_e)$ are the real and imaginary parts of $\varepsilon(T_e)$, respectively. Eq. **S2** is an excellent approximation to the full Mie solution for our system because the diameters of the particles under study (3.2–3.6 nm) are much smaller than the wavelength of the incident light (400–800 nm) (2, 3). We assume that the dielectric function of the ligand layer coating the nanoparticles is the same as that of the solvent (toluene). We also use the fact that the scattering contribution to the extinction coefficient is negligible, as shown in Fig. S4.

We described the dielectric constant $\varepsilon(T_e)$ with the model proposed by Scaffardi and Tocho (4), which is based on the work of Rosei et al. (5) and Inouye et al. (6). In this model, the dielectric function is given by the sum of the dielectric function of the free electrons and the dielectric function of the bound electrons (Eq. **S3**) as follows:

$$\varepsilon = \varepsilon_{free} + \varepsilon_{bound}. \qquad \textbf{[S3]}$$

The dielectric function of the free electrons due to intraband transitions near the Fermi level is given by the Drude model (Eq. **S4**) as follows:

$$\varepsilon_{free}(\omega, T_e) = 1 - \frac{\omega_p^2}{\omega^2 + i\gamma_{free}\omega}, \qquad \textbf{[S4]}$$

where ω is the frequency of the incident light, ω_P is the plasma frequency of Au, and γ_{free} is a damping parameter that depends on the size, surface chemistry, and electronic temperature of the NPs (4, 6, 7).

The dielectric function of the bound electrons originated from the electronic transitions from the d-band to the sp-band can be modeled by Eq. **S5** (4–7) as follows:

$$\varepsilon_{bound}(\omega, T_e) = Q_{bulk}\int_{\omega_g}^{\infty}\frac{\sqrt{x-\omega_g}}{x}[1 - F(x, T_e)] \times \frac{\left(x^2 - \omega^2 + \gamma_b^2 + i2\omega\gamma_b\right)}{\left(x^2 - \omega^2 + \gamma_b^2\right)^2 + 4\omega^2\gamma_b^2}dx, \qquad \textbf{[S5]}$$

where Q_{bulk} is the constant that determines the contribution of the bound electrons to the dielectric function, ω_g is the gap energy, γ_b is a damping parameter (that depends on the size, surface chemistry, and electronic temperature of the NP), and $F(x, T_e)$ is the Fermi–Dirac distribution (Eq. **S6**) as follows:

$$F(x, T_e) = \frac{1}{\exp\left(\frac{(\hbar x - \mu)}{kT_e}\right) + 1}, \qquad \textbf{[S6]}$$

where μ is the chemical potential of the electrons in Au.

We fit the GS absorption spectrum by minimizing the difference between the experimental spectrum and the spectrum simulated for T_e = 298 K (these calculations were performed with a home-written MATLAB program). We used the parameters C (Eq. **S2**), γ_{free}, and γ_b as fitting parameters, and the values tabulated in ref. 4 for the other parameters in Eqs. **S4–S6**. The best-fitting curves are shown in Fig. 1 in the main text. We find $\gamma_{free} = 6.74 \times 10^{14}$ for the aminated NPs, and 1.16×10^{15} for the thiolated NPs; $\gamma_b = 4.54 \times 10^{14}$ for the aminated NPs, and 5.33×10^{14} for the thiolated NPs at 298 K.

We simulated the TA spectrum for a given delay time as the difference between the absorption spectrum for the electronic temperature of the excited Au NPs, T_e, and the absorbance spectrum for T_e = 298 K. We then minimized the difference between the simulated and the measured TA spectra using T_e, $\gamma_{free}(T_e)$, and $\gamma_b(T_e)$ as the fitting parameters. In the fitting procedure, we fixed the values of C, γ_{free}(298 K), and γ_b(298 K) to those obtained from the fit of the GS absorption spectrum for the same sample (listed above). Fig. 2 in the main text shows the best fit of the experimental TA spectra for a series of delay times. Fig. S5 shows the best-fitting values of $\gamma_{free}(T_e)$ and $\gamma_b(T_e)$ vs. T_e for the aminated and thiolated samples at different pump powers. We observe that the relative change in the damping parameters [$|\Delta\gamma_{free}(T_e)/\gamma_{free}(298\text{ K})| < 6\%$ and $|\Delta\gamma_b(T_e)/\gamma_b(298\text{ K})| < 7\%$] is much smaller than the relative change in electronic temperature ($\Delta T_e/298\text{ K} < 400\%$), in good agreement with previous observations (6).

Analysis of the Hot Electron Cooling Dynamics. The dynamics of cooling of the hot electron population in metal NPs is modeled using the two-temperature model (2TM) (Eqs. **S7** and **S8**) (6, 8–22) as follows:

$$\gamma T_e\frac{dT_e}{dt} = -g(T_e - T_L) \qquad \textbf{[S7]}$$

$$C_L\frac{dT_L}{dt} = g(T_e - T_L), \qquad \textbf{[S8]}$$

where γT_e is the electronic heat capacity of the electron population (γ is the heat capacity coefficient), g is the electron–phonon coupling parameter, C_L is the heat capacity of the Au lattice, and T_L is the temperature of the lattice. We assume that T_L is the temperature at time 0 (T_0 = 298 K). We have neglected, in this equation, the dissipation of the lattice vibrational energy into the solvent bath because this process is much slower than the energy exchange between the electron and phonon populations.

There are two possible strategies to extract the electron–phonon coupling parameter using the 2TM: from the "intrinsic lifetime" (the first-order lifetime in the limit of zero-excitation power) or by fitting the kinetics of hot electron cooling (the T_e vs. time plot) with Eqs. **S7** and **S8**. We performed both methods, and compare them below.

(i) Determination of g from the intrinsic lifetime. Most works determine g from the intrinsic lifetime because this method does not require fitting the TA spectra with the temperature-dependent Mie theory, as we did in this work. This analysis involves two steps:

(i) Determining the electron cooling lifetime (τ) for a given excitation power (U): This step requires fitting the cooling

kinetics as a first-order (exponential) decay. Although the kinetics produced by Eqs. **S7** and **S8** are clearly non-first order, this approximation can be justified for very short times following excitation (see derivation of Eq. **S10** below). Note also that previous works where τ was determined from the ΔA vs. time kinetics (instead from the T_e vs. time kinetics) implicitly assumed a linear relationship between ΔA and T_e ($\Delta A = k \cdot T_e$).

(*ii*) Plotting τ vs. U and extrapolating to the zero power limit to get the intrinsic lifetime $\tau(U = 0) = \gamma T_0/g$. To derive the expression $\tau(U = 0) = \gamma T_0/g$, we assume $T_L \sim T_0$, and integrate Eq. **S7** to get Eq. **S9** as follows:

$$T_L \log\left(\frac{\Delta T_e}{\Delta T_e^{\max}}\right) + \left(\Delta T_e - \Delta T_e^{\max}\right) = \frac{gt}{\gamma}, \qquad \textbf{[S9]}$$

where $\Delta T_e = T_e - T_0$ and "max" indicates the temperature just after the excitation pulse. For small delay times, $\Delta T_e/\Delta T_e^{\max} \sim 1$ and $\log(\Delta T_e/\Delta T_e^{\max}) \sim 0$. A Taylor expansion around $\log(\Delta T_e/\Delta T_e^{\max}) = 0$ gives Eq. **S10** as follows:

$$\left(T_0 + \Delta T_e^{\max}\right) \log\left(\frac{\Delta T_e}{\Delta T_e^{\max}}\right) = \frac{gt}{\gamma}. \qquad \textbf{[S10]}$$

Eq. **S10** shows that, for small delay times, ΔT_e decays with first-order kinetics with a characteristic lifetime τ (Eq. **S11**),

$$\tau = \frac{\gamma\left(T_0 + \Delta T_e^{\max}\right)}{g} = \frac{\gamma T_0}{g} + \frac{\gamma \Delta T_e^{\max}}{g}, \qquad \textbf{[S11]}$$

that increases with the initial temperature; in other words, the cooling process slows as the excitation energy increases. The initial temperature and the excitation energy (U) are related by Eq. **S12** as follows:

$$U = \int_{T_0}^{T_e^{\max}} \gamma T_e dT_e = \frac{1}{2}\gamma\left(\left(T_e^{\max}\right)^2 - T_0^2\right) \approx \gamma \Delta T_e^{\max} T_0, \qquad \textbf{[S12]}$$

where we use the fact that, for a sufficiently small perturbation, $T_e^{\max} \approx T_0$. The combination of Eqs. **S11** and **S12** yields Eq. **S13** as follows:

$$\tau = \frac{\gamma\left(T_0 + \Delta T_e^{\max}\right)}{g} = \frac{\gamma T_0}{g} + \frac{U}{gT_0}, \qquad \textbf{[S13]}$$

which predicts that τ is a linear function of U (close to $U = 0$), and that the y-intercept and the slope of the plot of τ vs. U are $T_0\gamma/g$ and $U/(gT_0)$, respectively. We can therefore obtain g from the intercept or from the slope of the plot. Fig. 3*C* in the main text shows that τ is, in fact, a linear function of U; however, we found marked discrepancies between the values of g determined from the intercept, $(2.41 \pm 0.05) \times 10^4$ for aminated Au NPs and $(2.98 \pm 0.02) \times 10^4$ for thiolated Au NPs, and those determined from the slope: $(14 \pm 1) \cdot 10^4$ for aminated Au NPs and $(19 \pm 1) \cdot 10^4$ for thiolated Au NPs. This discrepancy suggests that (at least) one of the approximations involved in the derivation of Eqs. **S9–S13** is not fulfilled in our system. We believe that a major source of error is the determination of τ from the T_e vs. time traces, which should be evaluated for small delay times; however, at small delay times, the measured kinetics are strongly affected by the instrument response. We also show below that g depends on T_e; this dependence is not considered by the analysis discussed in this section.

(ii) Determination of g by fitting the T_e vs. time curves with the 2TM model equations (Eqs. S7 and S8). This analysis involves fitting the T_e vs. time curves with the differential equations of the 2TM; this method requires less manipulation of the experimental data than the intrinsic lifetime method, but also requires that we determine the T_e vs. time curves by fitting the TA spectra with a temperature-dependent Mie theory (as we did in this work).

Our attempts to fit the plots of T_e vs. time using the 2TM as written in Eqs. **S7** and **S8** with a temperature-independent value of g produced only medium-quality fits to the experimental data (Fig. S6). We can improve the quality of the fits by explicitly considering the dependence of g on the electronic temperature.

To incorporate a dependence of g on the electronic temperature, we considered successive Taylor expansions of g in terms of the difference between the electronic temperature T_e and the temperature of the lattice, $\Delta T = (T_e - T_L)$ (Eqs. **S14–S16**), as follows:

$$g = g_0 \qquad \textbf{[S14]}$$

$$g = g_0 + g_1 \Delta T \qquad \textbf{[S15]}$$

$$g = g_0 + g_1 \Delta T + g_2 \Delta T^2. \qquad \textbf{[S16]}$$

We then performed a global fit of the T_e vs. time curves for all powers and all samples of a given surface chemistry simultaneously (we performed a global fit) using Eqs. **S7** and **S8**, and the expression for g given by either Eq. **S14**, **S15**, or **S16**. We estimated the quality of these fittings by looking at the reduced sum of squares, defined in Eq. **S17** as follows:

$$\chi^2_{red} = \frac{1}{dof} \sum_i \left(Y_{pred}(i) - Y_{obs}(i)\right)^2, \qquad \textbf{[S17]}$$

where $Y_{pred}(i)$ and $Y_{obs}(i)$ are the predicted and observed values for point i (the summation runs over all of the points of all of the kinetic traces in the global fit), and *dof* is the number of degrees of freedom (the total number of points minus the number of fitting parameters).

Table S2 shows that using two fitting parameters ($g = g_0 + g_1\Delta T$; Eq. **S15**) decreases χ^2_{red} by more than a factor of three with respect to the fitting with one fitting parameter ($g = g_0$, Eq. **S14**), thus greatly improving the quality of the fit. The quality of the fitting is, however, only marginally improved by adding an additional fitting parameter (Eq. **S16**); therefore, we decided to use two fitting parameters (g_0 and g_1) in the global fit.

To summarize, we decided to analyze the T_e vs. time kinetics by fitting the experimental data with the differential equations of the 2TM (Eqs. **S7** and **S8**) and the temperature-dependent value of g given by Eq. **S15**, because (*i*) this analysis requires fewer approximations than the intrinsic lifetime approach; (*ii*) the intrinsic lifetime approach shows inconsistencies between the values calculated from the slope and the intercept of the τ vs. U plot. We note that the values of g_0 determined from the fitting with the 2TM in Table 1 in the main text are close to the value of g determined from the intercept of the τ vs. U plot in Table S2 (and therefore the intercept provides a more accurate estimation of g than the slope); and (*iii*) we obtained very good-quality fits of the experimental data to Eqs. **S7** and **S8** after the temperature dependence of g was taken into account.

Density Functional Theory Modeling. A slab of gold having the bulk structure (fcc) was passivated in four sites on the surface with either methylamine or ethylthiolate. In the methylamine case, the binding geometry found by Trout et al. for a gold surface

was used as a starting point for the geometry relaxation (23). In the case of ethylthiolate, ligands were bound to the (111) surface through a gold ad-atom in a "staple" motif, known to be an extremely stable binding arrangement for both Au (111) surfaces and Au nanoparticles (24, 25). Carbon and hydrogen atom positions were initially relaxed using molecular mechanics with the universal force field, as implemented in the Avogadro 1.1.0 software (26). Following relaxation of the C and H positions, the surfaces of the gold slab along with the ligands were relaxed using density functional theory (DFT). Gold atoms beneath the surface layer were frozen during geometry relaxations. All DFT calculations used the Amsterdam Density Functional (ADF) 2010.01 program (27). DFT-based geometry relaxations and electronic structure calculations made of use of the BP86-D GGA exchange correlation functional with a triple-zeta potential basis set with a single polarization function (TZP.4f). For gold atoms, a 4f frozen core approximation was used and scalar relativistic effects were incorporated using the zeroth-order regular approximation (28, 29). In all density of electronic states (DOS) plots, the system's HOMO (Fermi level at 0 K) has been set as the zero of energy. DOS stick spectra were broadened using a thermal broadening function having a width (σ) of 0.02 eV.

Simulation of the Electron–Phonon Coupling. The electron–phonon coupling [$g(T_e)$], like the electronic heat capacity, depends on the electronic DOS (30), as given in Eq. **S18**:

$$G(T_e) = \frac{\pi \hbar k_B \lambda < \omega^2 >}{DOS(\varepsilon_{fermi})} \int_{-\infty}^{\infty} \frac{df(\varepsilon, \mu, T_e)}{d\varepsilon} DOS^2(\varepsilon) d\varepsilon, \qquad \textbf{[S18]}$$

where $< \omega^2 >$ is the second moment of the phonon spectrum defined by McMillan and λ is the electron–phonon mass enhancement parameter; both parameters are material dependent and are assumed to be bulk Au values. The temperature dependence of the electron–phonon coupling in this expression is rationalized through the inclusion of electron scattering far from the Fermi level, which becomes relevant at high electron temperatures. The simulations in Fig. S7 show that the electron–phonon coupling constant is affected by the DOS near the Fermi level. Eq. **S18** reduces to a linear dependence of the electron–phonon coupling on the $DOS_{\text{Fermi level}}$ at 0 K, as the energy derivative of the Fermi–Dirac distribution becomes a delta function at the Fermi level. Note that several different functions can be used as an approximation of the chemical potential; however, we found that, in the temperature range used (298–5000 K), the chemical potential did not significantly deviate from the Fermi level. The simulated electron–phonon couplings shown in Fig. S7 are temperature dependent, but a direct comparison with the experimentally observed electron–phonon coupling is not appropriate because the Au slab model is not representative enough of the nanoparticle (for example, the ratio of ligands to Au atoms is significantly lower in the slab) to make the connection meaningful. For example, the bulk values used for λ and $< \omega^2 >$ would be expected to differ for the slab and an Au NP.

Effect of Energy Dissipation into the Solvent Bath on the Hot Electron Kinetics. As discussed by Hartland (31), heat dissipation from the Au lattice into the solvent can be separated into two processes as follows.

(i) Heat transfer at the Au NP/solvent interface. This process is described by Eq. **S19** as follows:

$$C_L \frac{\partial T_L(t)}{\partial t} = -\frac{3G}{R}\left(T_L(t) - T_s(t,R)\right), \qquad \textbf{[S19]}$$

where $T_L(t)$ is the temperature of the lattice at time t, $T_s(t,R)$ is the temperature of the solvent on the surface of the particle at time t, C_L is the lattice heat capacity per unit volume, and G is the interfacial conductivity. The characteristic timescale for this process is (31) given by Eq. **S20** as follows:

$$\tau_i = \frac{C_L R}{3G}. \qquad \textbf{[S20]}$$

For typical values of $G = 1{\cdot}10^8$ J·s^{-1}·m^{-2}·K^{-1}, $C_L = 2.49{\cdot}10^6$ J·K^{-1}·m^{-3}, and $R = 1.5$ nm, we get $\tau_I = 12.5$ ps.

(ii) Heat transport in the solvent. This process is given by Eq. **S21** as follows:

$$C_s \frac{\partial\left(rT_s(t,r)\right)}{\partial t} = \Lambda_s \frac{\partial^2\left(rT_s(t,r)\right)}{\partial r^2}, \qquad \textbf{[S21]}$$

where Λ_s is the thermal conductivity of the solvent (0.14 W·m^{-1}·K^{-1} for toluene) and C_s is the heat capacity of the solvent ($1.49{\cdot}10^6$ J·K^{-1}·m^{-3} for toluene). The characteristic timescale for heat transport in the solvent is given by Eq. **S22** (31) as follows:

$$\tau_P = \frac{(C_L R)^2}{9 C_S \Lambda_S}. \qquad \textbf{[S22]}$$

We find $\tau_P = 7.5$ ps. Note that heat transfer at the NP/solvent interface is slower than heat transport in the solvent, and therefore it is the rate-limiting step for heat exchange between the solvent bath and the metal nanoparticle. Therefore, the characteristic timescale of heat exchange between the solvent bath and the NP is in our system is ~12.5 ps, which is between 6 and 12 times larger than the timescale of electron–phonon coupling (1–2 ps). To demonstrate that energy dissipation into the solvent has a negligible effect on the kinetics of electron cooling, we explicitly included heat transfer at the NP/solvent interface in the 2TM (Eqs. **S23** and **S24**,) and simulated the electron cooling kinetics by fixing the values of g_0 and g_1 to those determined with the 2TM without dissipation into the bath (Eqs. **S7** and **S8**). Fig. S8 shows that including dissipation to the bath has a negligible effect in the electron cooling kinetics, and therefore it is not necessary to consider this process in the analysis.

$$\gamma T_e \frac{dT_e}{dt} = -(g_0 + g_1(T_e - T_L))(T_e - T_L) \qquad \textbf{[S23]}$$

$$C_L \frac{dT_L}{dt} = (g_0 + g_1(T_e - T_L))(T_e - T_L) - 3\frac{G}{R}(T_L - T_0). \qquad \textbf{[S24]}$$

1. Malicki M, et al. (2010) Excited-state dynamics and dye-dye interactions in dye-coated gold nanoparticles with varying alkyl spacer lengths. *Phys Chem Chem Phys* 12(23): 6267–6277.
2. Harris N, Blaber MG, Schatz GC (2012) Optical properties of metal nanoparticles. *Encyclopedia of Nanotechnology*, ed Bhushan B (Springer, Dordrecht, The Netherlands), Vol 481, pp 9751–9754.
3. Kelly KL, Coronado E, Zhao LL, Schatz GC (2003) The optical properties of metal nanoparticles: The influence of size, shape, and dielectric environment. *J Phys Chem B* 107(3):668–677.
4. Scaffardi LB, Tocho JO (2006) Size dependence of refractive index of gold nanoparticles. *Nanotechnology* 17(5):1309–1315.
5. Rosei R, Antonang F, Grassano UM (1973) D bands positions and width in gold from very low-temperature thermomodulation experiments. *Surf Sci* 37(1):689–699.
6. Inouye H, Tanaka K, Tanahashi I, Hirao K (1998) Ultrafast dynamics of nonequilibrium electrons in a gold nanoparticle system. *Phys Rev B* 57(18):11334–11340.
7. Comin A, Korobchevskaya K, George C, Diaspro A, Manna L (2012) Plasmon bleaching dynamics in colloidal gold-iron oxide nanocrystal heterodimers. *Nano Lett* 12(2): 921–926.
8. Ahmadi TS, Logunov SL, El-Sayed MA (1996) Picosecond dynamics of colloidal gold nanoparticles. *J Phys Chem* 100(20):8053–8056.
9. Busby M, Chiorboli C, Scandola F (2006) Relaxation dynamics and transient behavior of small arenethiol passivated gold nanoparticles. *J Phys Chem B* 110(12):6020–6026.

10. Groeneveld RHM, Sprik R, Lagendijk A (1995) Femtosecond spectroscopy of electron-electron and electron-phonon energy relaxation in Ag and Au. *Phys Rev B Condens Matter* 51(17):11433–11445.
11. Gu T, Ye T, Simon JD, Whitesell JK, Fox MA (2003) Subpicosecond transient dynamics in gold nanoparticles encapsulated by a fluorophore-terminated monolayer. *J Phys Chem B* 107(8):1765–1771.
12. Hartland GV (2004) Measurements of the material properties of metal nanoparticles by time-resolved spectroscopy. *Phys Chem Chem Phys* 6(23):5263–5274.
13. Hodak JH, Henglein A, Hartland GV (2000) Electron-phonon coupling dynamics in very small (between 2 and 8 nm diameter) Au nanoparticles. *J Chem Phys* 112(13):5942–5947.
14. Hodak JH, Martini I, Hartland GV (1998) Spectroscopy and dynamics of nanometer-sized noble metal particles. *J Phys Chem B* 102(36):6958–6967.
15. Hu M, Hartland GV (2002) Heat dissipation for Au particles in aqueous solution: Relaxation time versus size. *J Phys Chem B* 106(28):7029–7033.
16. Huang W, Qian W, El-Sayed MA, Ding Y, Wang ZL (2007) Effect of the lattice crystallinity on the electron–phonon relaxation rates in gold nanoparticles. *J Phys Chem C* 111(29):10751–10757.
17. Kamat PV (2002) Photophysical, photochemical and photocatalytic aspects of metal nanoparticles. *J Phys Chem B* 106(32):7729–7744.
18. Link S, El-Sayed MA, Gregory Schaaff T, Whetten RL (2002) Transition from nanoparticle to molecular behavior: A femtosecond transient absorption study of a size-selected 28 atom gold cluster. *Chem Phys Lett* 356(3–4):240–246.
19. Link S, et al. (2002) Hot electron relaxation dynamics of gold nanoparticles embedded in $MgSO_4$ powder compared to solution: The effect of the surrounding medium. *J Phys Chem B* 106(5):945–955.
20. Logunov SL, Ahmadi TS, El-Sayed MA, Khoury JT, Whetten RL (1997) Electron dynamics of passivated gold nanocrystals probed by subpicosecond transient absorption spectroscopy. *J Phys Chem B* 101(19):3713–3719.
21. Shin HJ, et al. (2003) Comparative investigation of energy relaxation dynamics of gold nanoparticles and gold–polypyrrole encapsulated nanoparticles. *J Phys Chem B* 107(20):4699–4704.
22. Westcott SL, Averitt RD, Wolfgang JA, Nordlander P, Halas NJ (2001) Adsorbate-induced quenching of hot electrons in gold core–shell nanoparticles. *J Phys Chem B* 105(41):9913–9917.
23. Pong B-K, Lee J-Y, and Trout BL (2005) First principles computational study for understanding the interactions between ssDNA and gold nanoparticles: Adsorption of methylamine on gold nanoparticulate surfaces. *Langmuir* 21(25):11599–11603.
24. Pensa E, et al. (2012) The chemistry of the sulfur-gold interface: In search of a unified model. *Acc Chem Res* 45(8):1183–1192.
25. Voznyy O, Dubowski JJ (2009) c(4x2) structures of alkanethiol monolayers on Au (111) compatible with the constraint of dense packing. *Langmuir* 25(13):7353–7358.
26. Hanwell MD, et al. (2012) Avogadro: An advanced semantic chemical editor, visualization, and analysis platform. *J Cheminform* 4(1):17.
27. Fonseca Guerra C, Snijders JG, te Velde G, Baerends EJ (1998) Towards an order-N DFT method. *Theor Chem Acc* 99(6):391–403.
28. van Lenthe E, Baerends EJ, Snijders JG (1993) Relativistic regular two-component Hamiltonians. *J Chem Phys* 99(6):4597–4610.
29. te Velde G, et al. (2001) Chemistry with ADF. *J Comput Chem* 22(9):931–967.
30. Lin Z, Zhigilei LV, Celli V (2008) Electron-phonon coupling and electron heat capacity of metals under conditions of strong electron-phonon nonequilibrium. *Phys Rev B* 77(7):075133.
31. Hartland GV (2011) Optical studies of dynamics in noble metal nanostructures. *Chem Rev* 111(6):3858–3887.

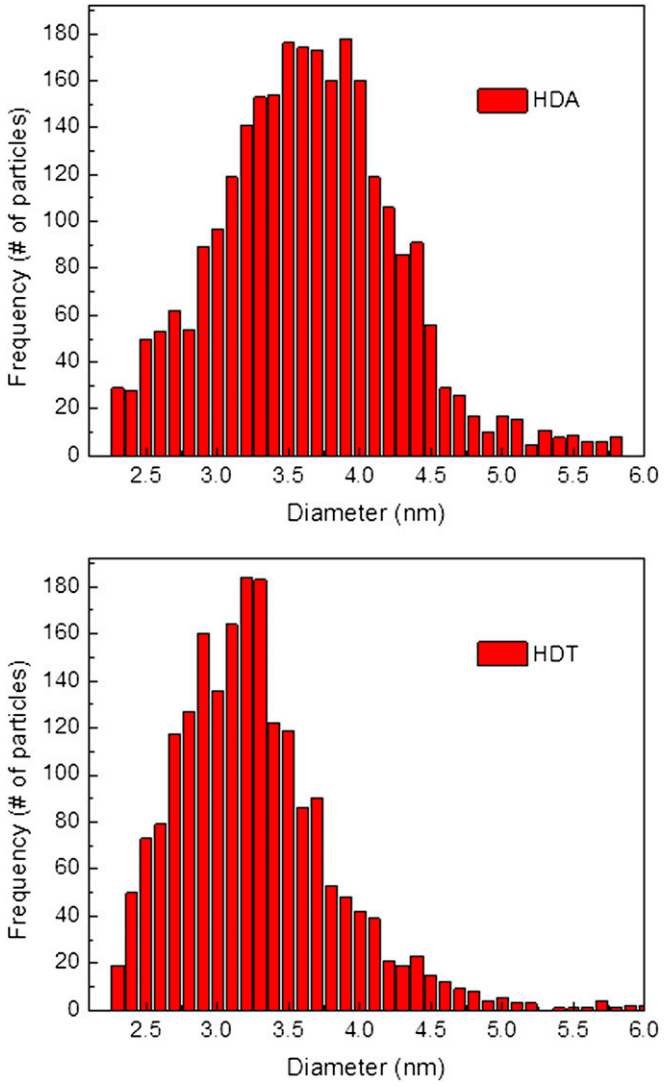

Fig. S1. Particle size distribution histograms for aminated (HDA) Au NPs (*Upper*) and thiolated (HDT) Au NPs (*Lower*), as determined by analysis of the TEM image.

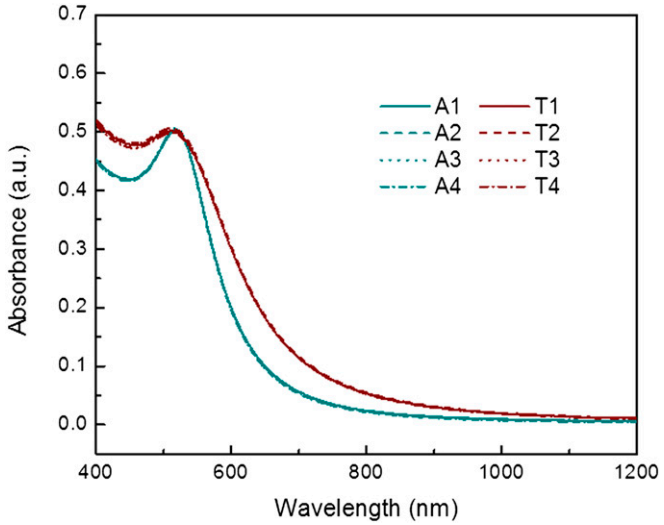

Fig. S2. Ground-state absorbance of Au NP samples (four replicates of each) used in the TA experiments. Aminated Au NP samples (A1–A4) are in cyan, and thiolated Au NP samples (T1–T4) are in maroon. All samples were diluted to an OD of ~0.5 a.u. with 10 mM HDA in toluene.

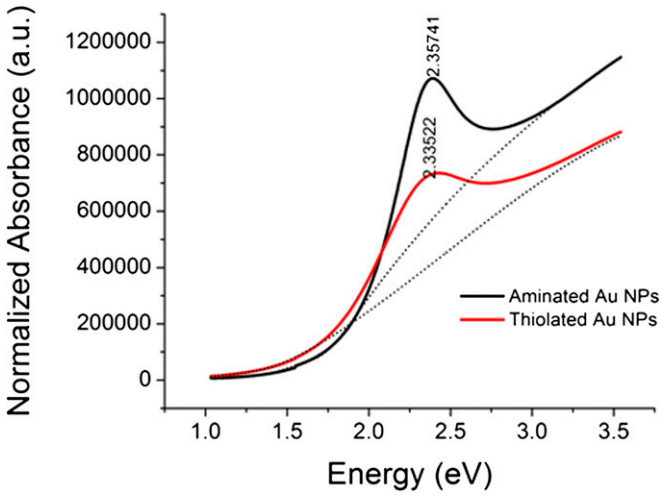

Fig. S3. The LSP absorption spectra for aminated and thiolated Au NPs, with peak energies of the LSP resonance indicated (2.36 eV for the aminated NPs, and 2.34 eV for the thiolated NPs).

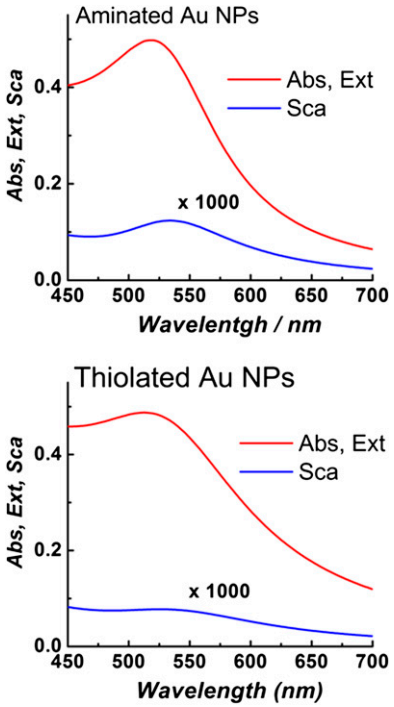

Fig. S4. Calculated extinction, absorption, and scattering spectra for the aminated and thiolated Au NPs. The extinction spectrum is not detectably different from the absorption spectrum.

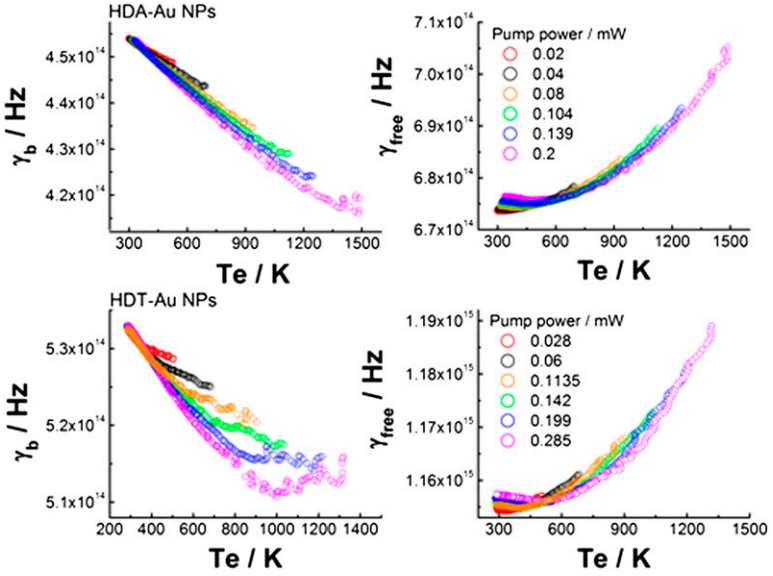

Fig. S5. Best-fitting values of the damping parameters $\gamma_{free}(T_e)$ and $\gamma_b(T_e)$ vs. T_e for the aminated (HDA) and thiolated (HDT) samples at the set of pump powers shown in the legend.

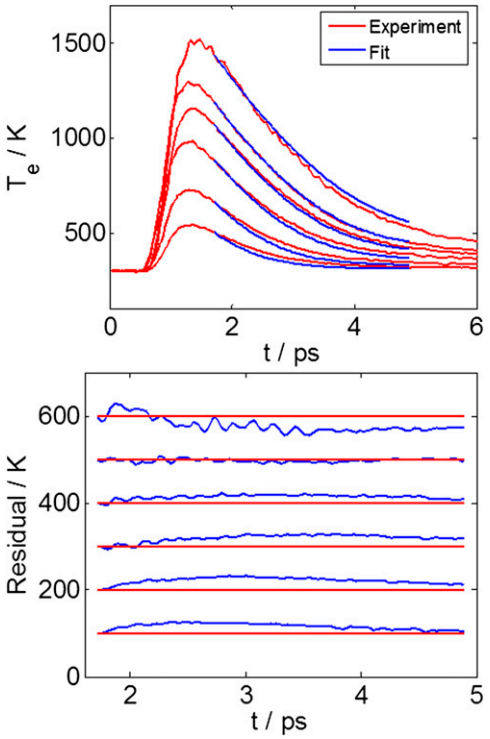

Fig. S6. (*Upper*) Measured electronic temperature vs. delay time for the aminated Au NPs at a series of pump energies, and best fits to these kinetics traces using the two-temperature model (Eqs. **S7** and **S8**) with a temperature-independent *g*. (*Lower*) Residuals of these fits.

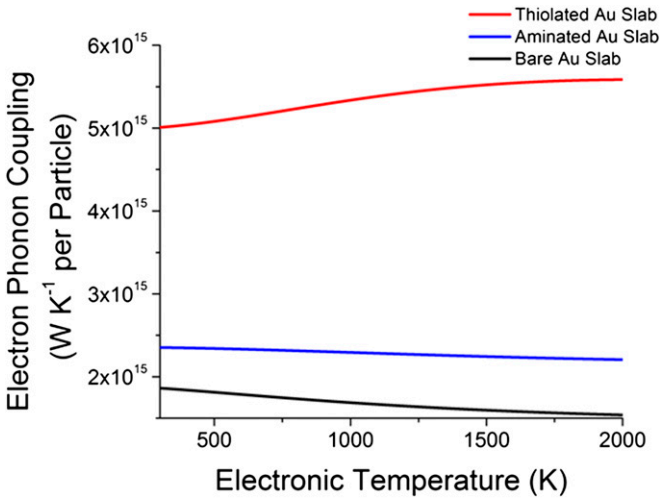

Fig. S7. Simulations of the electron–phonon coupling constant calculated with the electronic density of states determined by DFT of gold slabs. The thiolated Au slabs with higher DOS at the Fermi level show a larger electron–phonon coupling than both the aminated and bare Au slabs.

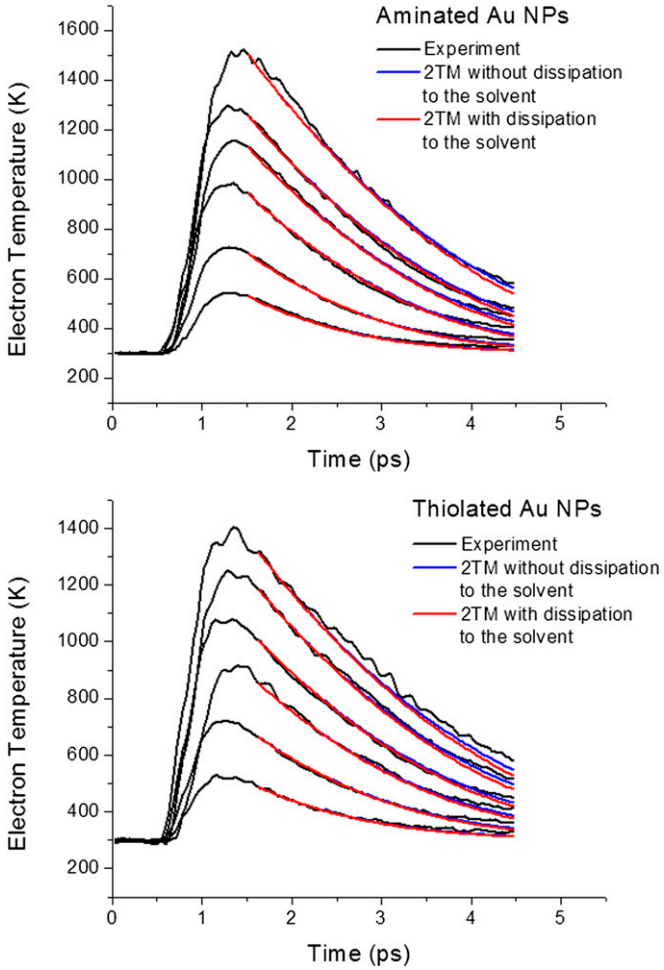

Fig. S8. Same plot as in Fig. 4 in the main text, but including a simulation of the 2TM that considers energy dissipation into the solvent bath (red curves). The 2TM with dissipation into the solvent bath is given by Eqs. **S23** and **S24**. In the simulation, we fixed the values of g_0 and g_1 to those obtained with the 2TM without energy dissipation (blue lines) and used $G = 1{\cdot}10^8$ J·s^{-1}·m^{-2}·K^{-1} and $R = 1.5$ nm. The figure shows that energy dissipation to the solvent has a negligible effect on the electron cooling kinetics in the time window of the fitting.

Table S1. Summary of Au NP LSPR properties by sample

Sample	λ^{max}, nm	ε (λ^{max}), M^{-1}·cm^{-1}
Aminated Au NPs		
A1	518	4.74×10^6
A2	518	4.71×10^6
A3	518	4.66×10^6
A4	518	4.73×10^6
Thiolated Au NPs		
T1	511	3.12×10^6
T2	511	3.05×10^6
T3	511	3.12×10^6
T4	511	2.98×10^6

Table S2. Values of χ^2 for additional temperature-dependent fitting parameters

No. of fitting parameters	HDA-AuNPs χ^2_{red}	HDT-AuNPs χ^2_{red}
One, $g = g_0$ (Eq. **S14**)	667	625
Two, $g = g_0 + g_1\Delta T$ (Eq. **S15**)	177	191
Three, $g = g_0 + g_1\Delta T + g_2\Delta T^2$ (Eq. **S16**)	126	173